PERGAMON

International Journal of Multiphase Flow 26 (2000) 549–581

International Journal of Multiphase Flow

www.elsevier.com/locate/ijmulflow

Validation of electrical-impedance tomography for measurements of material distribution in two-phase flows

D.L. George [a,*], J.R. Torczynski [a], K.A. Shollenberger [a], T.J. O'Hern [a], S.L. Ceccio [b]

[a] *Engineering Sciences Center, Sandia National Laboratories, Albuquerque, NM 87185-0834, USA*
[b] *Department of Mechanical Engineering and Applied Mechanics, University of Michigan, Ann Arbor, MI 48109-2121, USA*

Received 24 November 1998; received in revised form 20 April 1999

Abstract

A series of studies is presented in which an electrical-impedance tomography (EIT) system is validated for two-phase flow measurements. The EIT system, developed at Sandia National Laboratories, is described along with the computer algorithm used for reconstructing phase volume fraction profiles. The algorithm is first tested using numerical data and experimental phantom measurements, with good results. The EIT system is then applied to solid–liquid and gas–liquid flows, and radial phase volume fraction profiles within a circular cross-section are determined. These profiles are compared to results from an established gamma-densitometry tomography (GDT) system. In the solid–liquid flows, the average solid volume fractions measured by EIT are in good agreement with nominal values. In the gas–liquid flows, average gas volume fractions and radial gas volume fraction profiles from GDT and EIT are also in good agreement. Published by Elsevier Science Ltd.

Keywords: Electrical-impedance tomography; Bubble column; Gas volume fraction; Multiphase flow

1. Introduction

The spatial distribution of materials in multiphase flows is important to many chemical and industrial processes. For example, in indirect coal liquefaction, where a reactive gas is bubbled

* Corresponding author.

0301-9322/00/$ - see front matter Published by Elsevier Science Ltd.
PII: S0301-9322(99)00029-4

through a catalyst-laden slurry, a spatially nonuniform gas distribution within the reactor can reduce process efficiency by inducing large-scale, buoyancy-driven recirculating flows (Jackson et al., 1996). Techniques that measure the distribution of each phase in multiphase flows have the potential to improve the control of such processes. They also can be useful for validating computational models of multiphase flows (Plaskowski et al., 1995; Torczynski et al., 1997).

A dilemma encountered in multiphase flow measurements is that probes or instruments should be placed outside the flow domain so as not to disturb the flow itself; however, phase distributions cannot easily be measured from the boundary. Tomography offers a possible solution to this dilemma, and many different tomographic methods have been applied to the measurement of multiphase flows. Examples of these methods include gamma-densitometry tomography (GDT), electrical-impedance tomography (EIT), magnetic resonance imaging (MRI), acoustic tomography, and positron emission tomography (PET). Several of these methods were first derived for medical applications.

In this paper, GDT and EIT are applied to the task of providing spatially resolved information on dispersed multiphase flows. GDT and other radiation-based tomographic methods are relatively mature and can accurately measure spatial phase distributions (Hewitt, 1978; Shollenberger et al., 1997a). Their main disadvantage is that the data collection times required are usually longer than the time scales of time-dependent multiphase flows. EIT can acquire information much more quickly than GDT, but several issues with EIT have yet to be resolved, including its usefulness for multiphase flows, its spatial resolution, and its ability to make accurate quantitative measurements (Webster, 1990; Jones et al., 1993; Plaskowski et al., 1995; Ceccio and George, 1996). While capacitance sensors have been used to *visualize* gas–liquid slug flow (Huang et al., 1989) and flows in trickle-bed reactors (Reinecke and Mewes, 1997), the EIT technique must still be validated for *quantitative* phase volume fraction measurements.

This paper documents a series of studies in which an EIT system developed at Sandia National Laboratories and the University of Michigan (O'Hern et al., 1995; Torczynski et al., 1996a) and an established GDT technique at Sandia were used to quantify properties of two-phase flows. Since the GDT system has already been successfully applied to multiphase flows (Adkins et al., 1996; Torczynski et al., 1996b; Shollenberger et al., 1997a), it was used to assess the accuracy of the EIT system. The paper begins with a brief introduction to EIT theory and a description of the Sandia/Michigan EIT system. Numerical and experimental validation tests of the reconstruction algorithm are then presented. The final section of this paper describes the experimental conditions of the two-phase flow tests and compares results from EIT and GDT. Both solid–liquid flows and gas–liquid flows are examined.

2. Electrical-impedance tomography system

2.1. EIT theory

In electrical-impedance tomography, a number of electrodes are mounted to the surface of a domain of interest, **D**. As a prescribed current is injected into the domain at one electrode and withdrawn at another electrode, all electrode voltages are measured relative to ground (Fig. 1).

These measurements at the domain boundary are then used to reconstruct the impedance distribution within the domain and infer the phase distribution.

In practice alternating current (AC) is used to avoid polarization effects on the electrodes. For AC electrical conduction with field frequencies on the order of tens of megahertz or lower, the electric potential V within the domain **D** is related to the complex electrical conductivity γ of the domain by

$$\nabla \cdot \gamma \nabla V = 0. \tag{1}$$

Eq. (1) assumes that no charge sources or sinks are present in **D**. The boundary conditions on **D** are given by

$$\mathbf{n} \cdot \gamma \nabla V + j = 0, \tag{2}$$

where **n** is the unit normal vector outward from the domain boundary, and j is the charge flux on the boundary. Multiple measurements of j and V at the boundary are used to iteratively reconstruct the conductivity distribution within **D** that yields the measured boundary conditions.

In practice, current injections and voltage measurements are performed at a finite number of boundary locations (i.e., electrodes), and the limited resolution of the reconstructed conductivity field will be strongly related to the number and locations of the electrodes. If N electrodes are used, the domain can be modeled as an N-port impedance network, where a current source and current sink are placed on two of the ports, and the resulting voltage distribution around the network is measured at the remaining ports. One port, often the current sink, is referenced to ground. The total number of linearly independent voltage measurements R_N in the network is given by

$$R_N = \frac{N(N-1)}{2}. \tag{3}$$

R_N is also the number of independent impedance elements that can be determined from these voltage projections.

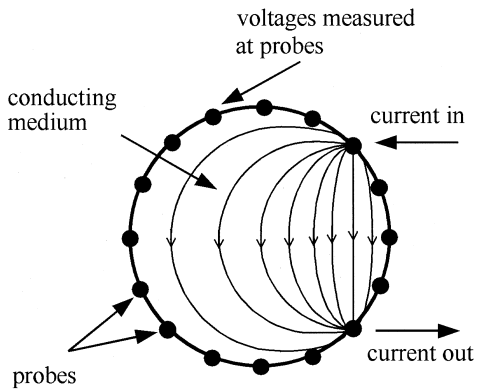

Fig. 1. Conceptual diagram of an EIT system applied to a circular domain.

To reconstruct the impedance distribution in the domain, a 'candidate' impedance distribution is first constructed. A set of voltage projections is then computed from the distribution and compared to voltages measured on the boundary during current injection. Next, the candidate impedance distribution is modified based on the difference between computed and measured voltages, and a new set of voltage projections is computed. This process continues until some minimum error criterion is satisfied. EIT reconstruction is an ill-conditioned problem; as a result, the reconstructed impedance 'solution' will be sensitive to noise in the projections and may not satisfy requirements of existence or continuous dependence on the problem data. The ill-conditioning and the sensitivity to noise increase as the number of electrodes and the spatial resolution of the solution increase. When available, a priori information about features of the impedance distribution may be used to aid in reconstruction (as is the case for the vertical multiphase flows examined here).

Several simplifications are generally employed in EIT that make it possible to reconstruct the impedance distribution in the domain using discrete finite-element methods (FEM). One common assumption is that current travels only in a two-dimensional domain. While three-dimensional current flow has been used for some elementary cases, including the vertical bubble-column flows in this work, full three-dimensional EIT reconstruction would require computational effort and resources that are impractical at this time. Another common simplification involves representing the conductivity by a piecewise constant function (e.g., a constant within each element of a finite element mesh). This approach is not followed here; instead, the conductivity is represented as a global function of position and of several conductivity parameters, as discussed later. By using a global conductivity function, regularization is implicitly included in the solution procedure, so no additional regularization is needed. It is also assumed in EIT that the impedance distribution within the domain does not change significantly over time while voltage projections are acquired. As a result, EIT systems must acquire projections rapidly, on time scales shorter than the characteristic time scales of multiphase flows. If this cannot be achieved (as with the vertical multiphase flows examined here), the uncertainty introduced by temporal averaging of voltages prior to reconstruction must be quantified. This is discussed in greater detail in Section 4.3.

A further simplification is achieved by assuming that resistive effects dominate over capacitive effects. An appropriate criterion can be obtained by separating the complex conductivity in Eq. (1) into its real and imaginary components (see, for example, Somersalo et al., 1992):

$$\gamma = \sigma + i2\pi f \tilde{\varepsilon}\varepsilon_0. \tag{4}$$

Here, σ is the DC (or real) conductivity, $\tilde{\varepsilon}$ is the normalized permittivity (or dielectric constant) of the medium, ε_0 is the permittivity of a vacuum (8.85×10^{-12} F/m), and f is the AC frequency. For resistance to dominate in the multiphase flows considered here, the following constraint on the liquid conductivity must be satisfied:

$$\sigma_L \gg 2\pi f \tilde{\varepsilon}_L \varepsilon_0. \tag{5}$$

For $f = 50$ kHz applied to water, for which $\tilde{\varepsilon}_L \approx 80$, this constraint is satisfied if $\sigma_L \gg 2$ μS/cm. This condition is often met by tap water and can also be attained by adding electrolytes to

deionized water. In this work, sodium nitrate was added to deionized water to ensure that liquid conductivities were at least 100 times higher than this limit. In the remainder of this work, resistive effects are assumed to dominate over capacitive effects in all experiments and calculations.

More information on EIT theory and the development of EIT systems for the study of multiphase flows may be found in the literature (Dickin et al., 1993; Jones et al., 1992, 1993, 1994; Ceccio and George, 1996).

2.2. FEM for reconstruction of conductivity distributions

The reconstruction algorithm used with the Sandia EIT system has been described in detail by Torczynski et al. (1996a, 1997) and is based on the YWT method described by Yorkey et al. (1987). This section summarizes the method (see also Fig. 2).

In the algorithm, the medium is treated as purely resistive, with no capacitive contribution; thus, $\gamma \rightarrow \sigma$ in Eqs. (1) and (2). The medium is surrounded by an insulating boundary through

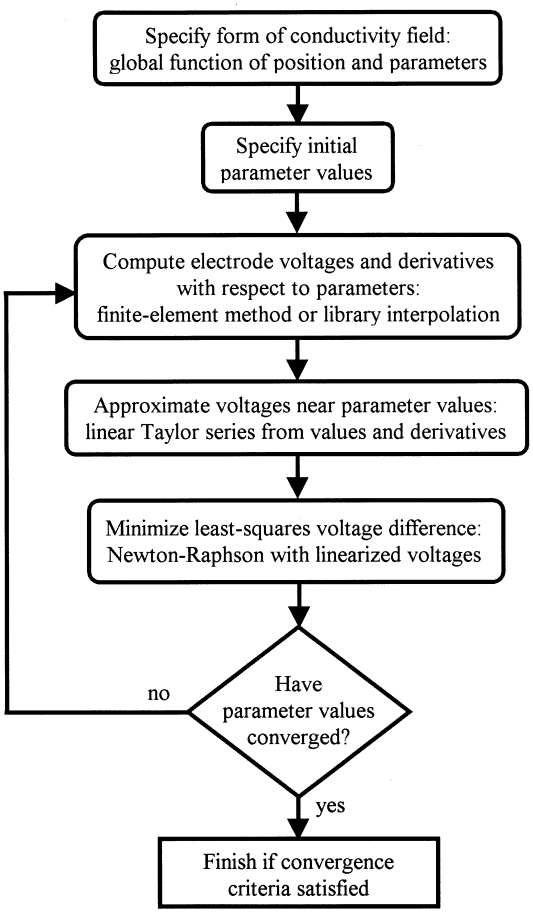

Fig. 2. Flow chart of EIT reconstruction algorithm.

which current is injected or withdrawn at discrete electrodes. An FEM representation is generated for the voltage equation, identical in form to the steady-state heat-conduction equation. Unlike most FEMs, the conductivity is not represented by a piecewise constant function that is discontinuous at element boundaries. Instead, the electrical conductivity is represented as a global function of position and of one or more conductivity parameters. For the boundary conditions, current flow is specified at the electrodes such that the net current into and out of the domain is zero.

The finite-element equations generated from Eqs. (1) and (2) are solved to find both the predicted voltages at the electrodes and the derivatives of the electrode voltages with respect to the conductivity parameters. Since no voltages are prescribed in the computational boundary conditions, the computed voltage solution of Eq. (1) is unique only to within an arbitrary additive constant. Subsequently, the conductivity parameters are adjusted by a Newton–Raphson algorithm to minimize the least-squares difference between the computed and experimental electrode voltages at the non-current-bearing electrodes. The value of the additive constant is determined during the least-squares minimization process.

Two computer codes have been written to implement this approach. The code FEMEIT models arbitrary two-dimensional domains and represents electrodes by mesh nodes, essentially mathematical points of zero width. FEMEIT generates and solves the FEM equations using global conductivity functions from a subroutine library and applies the Newton–Raphson algorithm to determine the final conductivity parameters. Conductivity functions in the library include a constant conductivity, a circular insulating region at an arbitrary position, and various analytical conductivity distributions.

The code EITAXI models cylindrical domains within which the conductivity varies only radially, but the voltage fields vary three-dimensionally due to the finite axial extent of the electrodes. The electrodes are taken to be identical and positioned at equal azimuthal intervals around the cylindrical domain. Unlike FEMEIT, EITAXI represents each electrode with its actual shape, rather than as a mathematical point. The conductivity field is represented as a global function of radial position and of conductivity parameters. Rather than solving the three-dimensional finite-element representation of the voltage field directly, as FEMEIT does in the two-dimensional case, EITAXI uses library files that contain the fundamental electrode voltages at discrete values of the conductivity parameters (Torczynski et al., 1996a, 1997). These library files are computed in advance using the commercial finite-element code FIDAP (Fluid Dynamics International, 1995). A cubic-spline interpolation is used to determine the fundamental electrode voltages for intermediate values of the conductivity parameters. The least-squares difference between the experimental voltages and appropriate linear combinations of the fundamental voltages is determined. A Newton–Raphson algorithm is then used to determine the values of the conductivity parameters that minimize this least-squares difference. EITCON, a simplified version of EITAXI, uses a uniform distribution across the domain and solves for the conductivity directly (no iterations are required).

Various conductivity distributions have been employed to date in both codes. These include a symmetric second-order (parabolic) polynomial in the radius r and a cylindrical insulating inclusion centered in the domain. The parabolic radial profile takes the form

$$\frac{\sigma}{\sigma_L} = \frac{1 + c\left[2(r/R)^2 - 1\right]}{b}, \tag{6}$$

where σ_L is the liquid conductivity, b is the conductivity scale parameter, c is the conductivity shape parameter, r is the radial cylindrical coordinate, and R is the domain radius (e.g., the bubble column radius).

As part of the axisymmetric reconstruction process, a set of nondimensional, fundamental voltage solutions $\{V_0, \ldots, V_{N/2}\}$ is generated. The supplementary computer code EITFUN was written to compute fundamental voltage solutions from axisymmetric experimental data sets, the reverse of the usual process. Comparisons of the computational and experimental fundamental solutions for no-flow conditions allowed an evaluation of different electrode geometries, the results of which are described in Section 2.4.

2.3. Determination of volume fraction from conductivity

A constitutive model is required to relate the electrical conductivity to the conducting and insulating phase volume fractions. When the continuous liquid phase is the only conducting phase, the Maxwell–Hewitt relation (Maxwell, 1881; Hewitt, 1978) can be used to relate the mixture conductivity σ and the liquid conductivity σ_L to the liquid volume fraction ε_L:

$$1 - \varepsilon_L = \frac{1 - [\sigma/\sigma_L]}{1 + \frac{1}{2}[\sigma/\sigma_L]} \quad \text{(three-dimensional inclusions)}. \tag{7}$$

Eq. (7) assumes three-dimensional inclusions of an insulating phase dispersed in a conducting phase (e.g., bubbles or insulating solid particles in salt water) and is applied locally in all tomographic reconstructions herein. An analogous relation can be derived for the somewhat artificial case of two-dimensional insulating inclusions dispersed in a conducting phase (e.g., parallel insulating posts in salt water):

$$1 - \varepsilon_L = \frac{1 - [\sigma/\sigma_L]}{1 + [\sigma/\sigma_L]} \quad \text{(two-dimensional inclusions)}. \tag{8}$$

Eq. (8) is not used in any of the tomographic reconstructions in this work, but is used to assess the amount of uncertainty introduced into the reconstructions by this type of constitutive model.

To assess the accuracy of the Maxwell–Hewitt relations (Eqs. (7) and (8)), the computational fluid dynamics code FIDAP was used to perform simulations of the voltage field in various multiply periodic geometries. Two-dimensional square lattices of insulating squares and circles and three-dimensional simple-cubic lattices of cubes and spheres were examined, where the region outside the insulating inclusion was filled with a uniformly conducting medium. Because of the symmetry and periodicity of these geometries, the computational domain consisted of only one quadrant of a two-dimensional unit cell or only one octant of a three-dimensional unit cell. In each case, the computational domain had a side length of unity and a conductivity of unity outside the insulating inclusion. Voltages of zero and unity were applied on two opposing sides of the domain, and insulating conditions were applied on the remaining sides by

virtue of symmetry. In the absence of an insulating inclusion (i.e., when the domain is simply a conducting square or cube), these conditions lead to a current of unity passing through the domain along one of its principal directions. When an inclusion is present, the current is reduced from this value by the ratio of the effective conductivity σ to the actual conductivity σ_L (per Ohm's Law).

Fig. 3 compares these effective conductivity ratios with the values predicted by the Maxwell–Hewitt relations for two- and three-dimensional insulating inclusions. The symbols represent FIDAP results, which are the exact solutions for converting conductivity measurements to insulating volume fractions. The dashed lines are values predicted by Eqs. (7) and (8). The upper bound, determined by the limiting case where current travels through a single layer of liquid and a single layer of gas arranged in parallel, is plotted as the solid line. It can be seen that using the Maxwell–Hewitt relations for insulating objects of these shapes will cause the insulating phase volume fraction to be only slightly overestimated. The results for circles and spheres closely follow the Maxwell–Hewitt relations until the inclusions touch. It is concluded that these relations are of uniformly good accuracy so long as inclusions are not highly distorted and can 'fill space without overlapping.'

The Maxwell–Hewitt relation has been shown to be reasonably accurate for monodisperse bubble-size distributions. However, in churn-turbulent bubble-column flow, there may be a bimodal distribution of bubble sizes, with many small bubbles and some large bubbles. Thus, it is important to quantify the errors that result from applying the monodisperse Maxwell–Hewitt

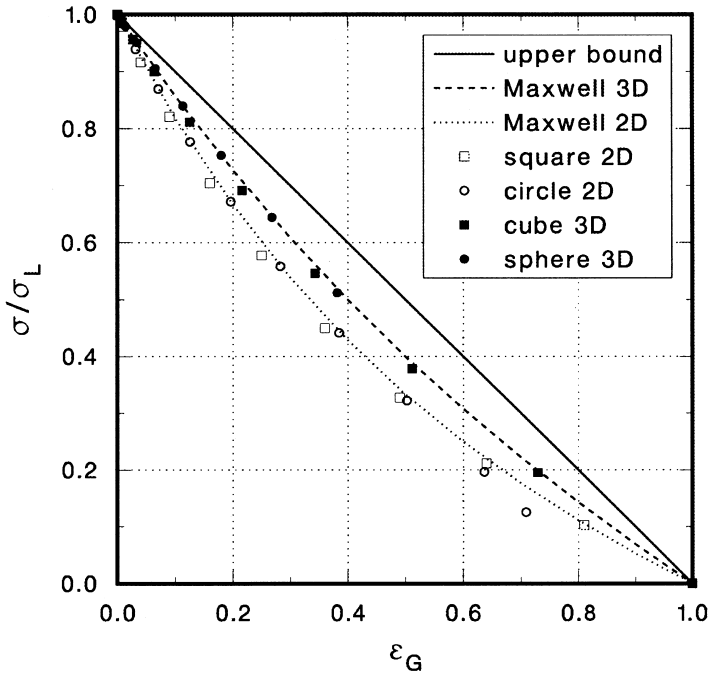

Fig. 3. Comparison of effective conductivities computed by FIDAP with predictions from the Maxwell–Hewitt relations.

relation to this situation. To this end, a bimodal distribution of bubbles is examined, for which the ratio of bubble diameters is large compared to unity. Since its accuracy has been demonstrated, the Maxwell–Hewitt relation is used recursively in this analysis to determine the effective conductivity of this medium.

Consider a mixture of a liquid of conductivity σ_L and an insulating gas. The gas has a total volume fraction of ε_G and is distributed in the form of 'large' bubbles, which have a volume fraction of $f\varepsilon_G$, and 'small' bubbles, which have a volume fraction of $(1-f)\varepsilon_G$. The large-bubble fraction f obeys the constraint $0 \leq f \leq 1$. The Maxwell–Hewitt relation can be applied recursively to determine the effective conductivity of this medium. The liquid and the small bubbles form a mixture denoted as medium A, with an effective conductivity σ_A given by

$$\frac{\sigma_A}{\sigma_L} = \frac{1-\varepsilon_A}{1+\frac{1}{2}\varepsilon_A}, \tag{9}$$

where

$$\varepsilon_A = \frac{(1-f)\varepsilon_G}{1-f\varepsilon_G}. \tag{10}$$

The large bubbles and medium A form another mixture denoted as medium B (bimodal), with an effective conductivity σ_B given by

$$\frac{\sigma_B}{\sigma_A} = \frac{1-\varepsilon_B}{1+\frac{1}{2}\varepsilon_B}, \tag{11}$$

where

$$\varepsilon_B = f\varepsilon_G. \tag{12}$$

These relations can be combined to determine the effective conductivity of the bimodal bubble mixture in terms of the total gas volume fraction ε_G and the fraction f of the gas in large bubbles, the bimodal Maxwell–Hewitt relation:

$$\frac{\sigma_B}{\sigma_L} = \left[\frac{1-f\varepsilon_G}{1+\frac{1}{2}f\varepsilon_G}\right]\left[\frac{1-\varepsilon_G}{1-\frac{3}{2}f\varepsilon_G+\frac{1}{2}\varepsilon_G}\right]. \tag{13}$$

When $f=0$ or $f=1$, this expression reduces to the monodisperse Maxwell–Hewitt relation, essentially Eq. (7):

$$\frac{\sigma}{\sigma_L} = \frac{1-\varepsilon_G}{1+\frac{1}{2}\varepsilon_G}. \tag{14}$$

For any value of f between 0 and 1, the bimodal curve lies slightly beneath the monodisperse curve. Thus, the assumption of a monodisperse bubble-size distribution in the presence of a

bimodal bubble-size distribution would cause the gas volume fraction to be slightly overpredicted. The large-bubble fraction at which the maximum difference between the monodisperse and bimodal Maxwell–Hewitt relations occurs for a given gas volume fraction ε_G is given by:

$$f_{max} = \frac{1 - \sqrt{1 - \varepsilon_G}}{\varepsilon_G}. \tag{15}$$

Evaluating the bimodal Maxwell–Hewitt relation at $f = f_{max}$ and comparing the resulting relation with the monodisperse Maxwell–Hewitt relation enables determination of the maximum possible error in gas volume fraction $\Delta\varepsilon_{G,max}$ as a function of true gas volume fraction ε_G. The error $\Delta\varepsilon_{G,max}$ never exceeds 0.028, the value at $\varepsilon_G = 0.723$, and is less than 0.01 for $\varepsilon_G \leq 0.3$. Since this degree of uncertainty is comparable to the uncertainty of the monodisperse Maxwell–Hewitt relation itself, it appears that bubble-size distribution does not significantly affect the accuracy of the Maxwell–Hewitt relation.

2.4. Sandia EIT system

A block diagram of the EIT system (Torczynski et al., 1997; George et al., 1998) is shown in Fig. 4. The system consists of an electrode array; a signal generator; a voltage-controlled current source; multiplexers connecting the electrode array to the current source, ground, and measurement electronics; an instrumentation amplifier and phase-sensitive demodulators; a low-pass filter to eliminate high-frequency components from the demodulated signals; and a data acquisition card. The data acquisition card contains an analog-to-digital converter that measures the DC signal components, and a digital controller that can be used to select

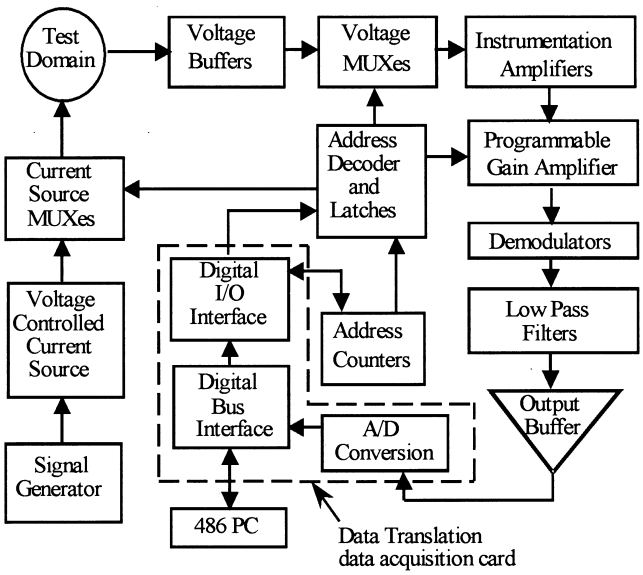

Fig. 4. Block diagram of Sandia/Michigan EIT system.

electrodes for current injection, ground, and measurement. The card also acts as an interface to a PC that operates the entire system.

During operation, the EIT system injects a controlled current through one electrode, 'sinks' a second electrode to ground, and measures voltages at all electrodes relative to ground. For completeness, a 'projection set' consists of measurements at all N electrodes for each injection and ground combination, for a total of $N^2(N-1)/2$ voltage measurements. Note that this is a factor of N greater than the number of independent pieces of information R_N; the extra information is used to reduce the impact of noise on the reconstructions. The domain is excited with a 50-kHz AC electric field. As demonstrated in Section 2.1, the resistive component of impedance dominates at this frequency for the air–water and polystyrene–water flows considered here.

The voltage signal from each electrode passes through an amplifier to a pair of phase-sensitive demodulators that separate the measured signal into two components: one demodulator produces the component in phase with the EIT carrier signal, the other yields the component out of phase with the carrier by 90°. Because the demodulators multiply two 50 kHz signals together (the measured voltage and the carrier or quadrature reference signal), their outputs consist of a 100 kHz sine wave superimposed on a DC component. The sine wave is removed by the low-pass filter, yielding the DC component proportional to the carrier or quadrature component of the measured voltage.

Commands issued to the multiplexers determine which electrodes are selected for current injection, grounding, and voltage measurement. Originally, the software issued these commands through the data acquisition card's digital controller. Later, integrated circuit (IC) counters were added to the EIT hardware to select injection, ground, and measurement electrodes in sequence. For 16 electrodes, the acquisition time for each voltage projection set was reduced from 2.7 s with the software command option to less than 0.75 s with IC counters. For this reason, the software-controlled option is called 'slow mode,' while the IC-controlled option is referred to as 'fast mode.' Validation tests presented in Section 3 demonstrated that the use of either mode has little impact on reconstruction accuracy.

The electrode array discussed in this paper was fabricated for use both in validation tests and in experiments conducted in a transparent bubble column. Sixteen electrodes were fashioned from stainless steel strips 0.64 cm wide, 7.62 cm high, and 76 μm thick. These were mounted at equal azimuthal intervals in a Lucite cylinder with an inner diameter of 19.05 cm, a wall thickness of 0.64 cm, and a height of 12.7 cm (Fig. 5). Other electrode arrays with square and circular electrodes 1.27 cm across were used during some preliminary experiments in order to evaluate the merits of different electrode geometries. The evaluation used measurements from each electrode ring with only liquid present in the domain (i.e., no gas flow). Fundamental voltage solutions, described in Section 2.2, were derived from these data sets with EITFUN and compared to computed solutions from FIDAP for the actual three-dimensional geometry (Table 1). The fundamental voltages from the square and circular electrode data were in poor agreement with calculated values; at all non-current-bearing electrodes the experimental voltages were similar. Besides implying a potential for significant disagreement between actual and calculated conductivity profiles, this similarity indicated that under multiphase flow conditions, the electrodes would have poor sensitivity to variations in the conductivity profile. In contrast, the fundamental voltage solutions from strip electrode

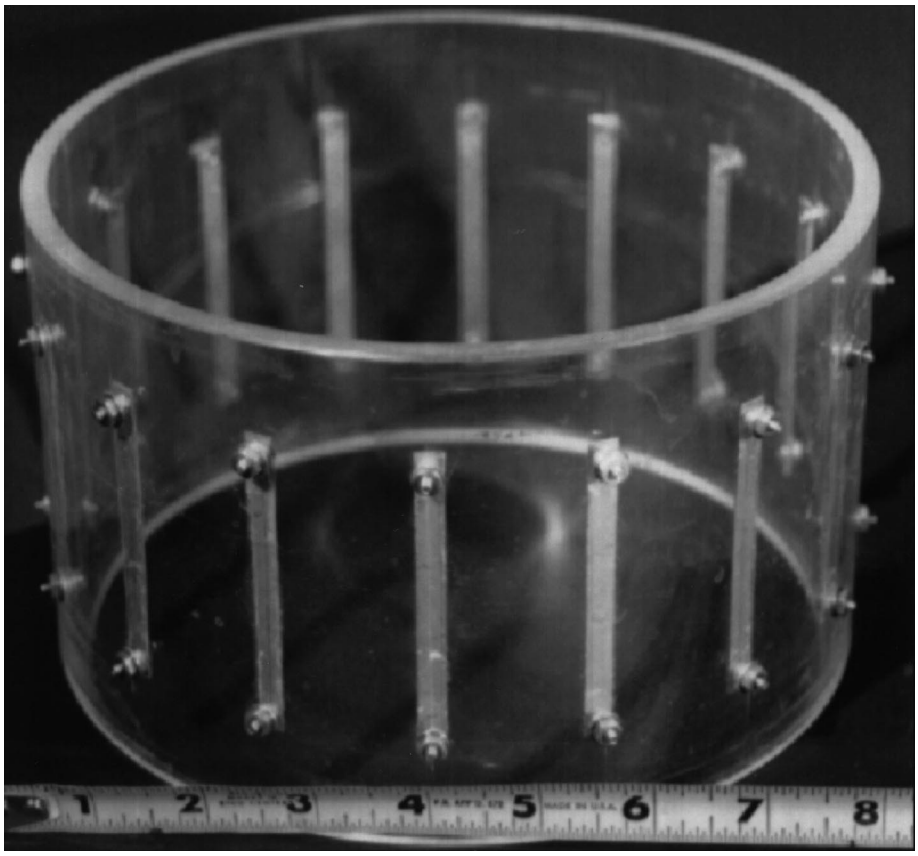

Fig. 5. EIT strip electrode array. The bottom scale is in inches.

Table 1
Fundamental voltage solutions for 16 strip electrodes in the transparent bubble column

Fundamental voltage	Computational value	Experimental value
V_0 (reference)	0	0
V_1	0.002275	0.002295
V_2	0.009430	0.009481
V_3	0.02260	0.02252
V_4	0.04432	0.04392
V_5	0.08030	0.07963
V_6	0.1454	0.1443
V_7	0.2947	0.2930
V_8 (current-bearing)	1.327	1.232

data were in excellent agreement with the computational values at the non-current-bearing electrodes 0 through 7 (Table 1). Although the voltages at the current-bearing electrode (V_8) differ somewhat, the reconstruction algorithm does not use this quantity (Torczynski et al., 1996a, 1997). The voltages at non-current-bearing electrodes varied significantly from one electrode to the next, implying a higher sensitivity to changes in the domain conductivity profile. Multiplying the experimental values by 1.007 brings them into agreement with computed voltages to almost three significant figures. A systematic difference of 0.7% between computational and experimental voltages is reasonable, since experimental accuracy in measurements of injected current and liquid conductivity is about $\pm 0.5\%$ and computational accuracy is similar. Based on these results, strip electrode data were used exclusively to reconstruct radial profiles of the multiphase flows.

3. Validation of reconstruction algorithm

3.1. Numerical validation of conductivity reconstruction algorithm

Several calculations were performed to validate the reconstruction algorithm. The first test involved an analytical result for the two-dimensional voltage distribution $V(x,y)$ in a circular domain of constant conductivity σ. The boundary conditions were defined by a current per unit length, J, injected at the boundary point (x_0,y_0) and withdrawn at the boundary point $(x_0, -y_0)$; this yielded the analytical result

$$V(x,y) = \left(\frac{J}{2\pi\sigma}\right)\ln\left[\frac{(y_0+y)^2+(x_0-x)^2}{(y_0-y)^2+(x_0-x)^2}\right]. \tag{16}$$

The uniform domain was bounded by 16 electrodes located at equal intervals of 22.5° around the perimeter. The radius of the circular domain, the current per unit length J, and the conductivity σ were all set to unity. By rotating the coordinates of the analytical results from selected injection and withdrawal combinations, the boundary voltages for all possible injection and withdrawal pairs were determined from the analytical solutions. These analytical voltages were input to FEMEIT, along with mesh information, to find the effect of mesh size on reconstruction accuracy. The conductivity function was chosen to be a single unknown

Table 2
Effect of FEMEIT mesh refinement on reconstruction accuracy of a uniform domain[a]

Mesh	Number of nodes	Number of elements	Computed σ
A	25	32	1.0443
B	81	128	1.0122
C	169	288	1.0047
D	289	512	1.0023
E	441	800	1.0013

[a] Analytical solution is $\sigma = 1$..

constant throughout the domain. Table 2 shows the dependence of the constant conductivity determined by FEMEIT for five meshes of appreciably different nodal density; an ideal result would be a calculated conductivity of unity. In all cases the calculated result is close to unity, and is converging to unity with increasing nodal density (Torczynski et al., 1996a).

In the second set of validation calculations, the finite-element code FIDAP was used to compute the boundary voltages corresponding to the synthetic spatial conductivity distribution shown in Fig. 6. This distribution mimics a bubble-column flow with an excess of bubbles in the upper right quadrant. The electrode geometry was identical to that used in the first problem. A highly refined mesh was used to guarantee that the FIDAP solution would be mesh-independent. The computed voltages from FIDAP were input to FEMEIT to test its ability to reproduce the original conductivity distribution, and reconstructions were performed using the same five meshes used in the first calculation set (Table 2).

Fig. 7 shows the most refined mesh used for this simulation (mesh E of Table 2) and the reconstructed conductivity field produced by the EIT algorithm for this mesh. Agreement is seen to be good. To quantify the effect of mesh refinement on reconstruction accuracy, average and rms conductivity values were computed for the FEMEIT results on each mesh and are listed in Table 3. As the mesh is refined, the average conductivity approaches the analytical average value of 2/3, and the rms value tends to zero.

3.2. Experimental validation of reconstructed conductivity profiles

The next step in validating the algorithm involved experimental data. Validation experiments were performed by capping the bottom of the cylinder containing the electrode array (Fig. 5)

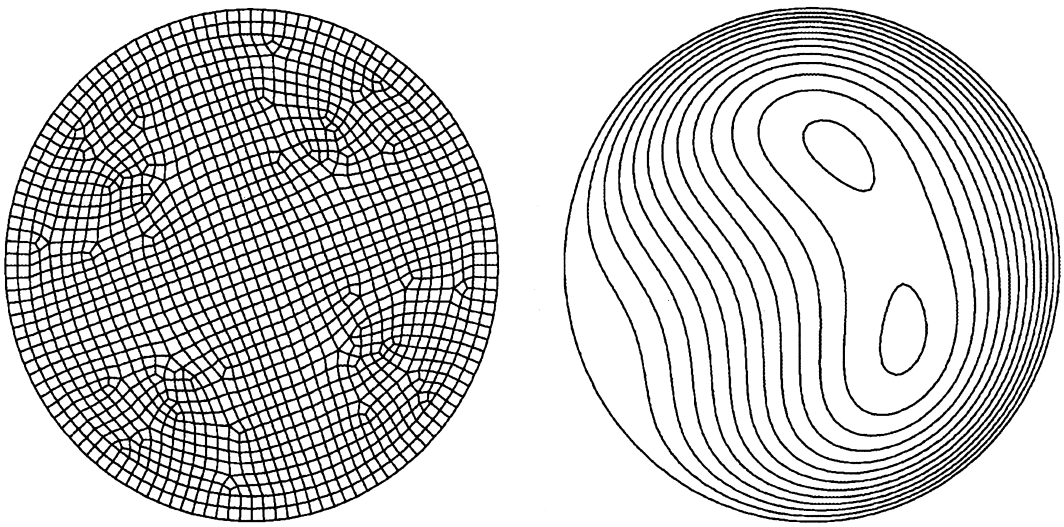

Fig. 6. Finite-element mesh used by FIDAP in validation tests (left) and synthetic benchmark conductivity field (right).

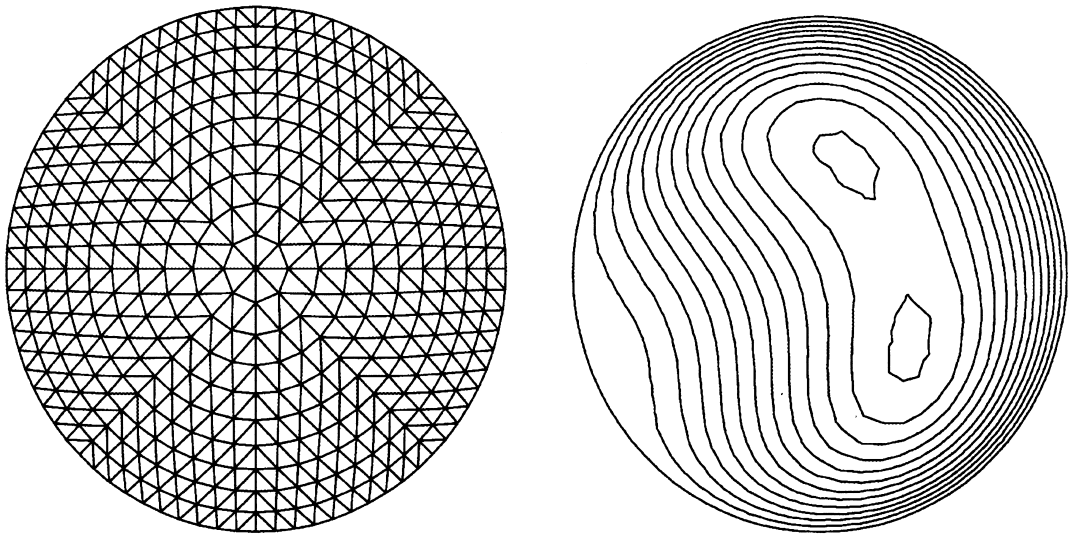

Fig. 7. Finite-element mesh used by FEMEIT in validation tests (left) and reconstructed conductivity field (right).

to form a static testbed, filling the testbed with a saltwater solution of known conductivity, and placing smaller Lucite cylinders of known radii in the testbed to act as insulating inclusions. EIT voltage measurements were then taken of the domain and used to reconstruct the location and position of the insulating 'phantom.' This configuration has been studied extensively by other investigators (e.g., Duraiswami et al., 1997). To limit the test domain in the vertical direction, the free surface of the liquid and the bottom Lexan end cap were aligned with the top and bottom ends of the strip electrodes, respectively. This eliminated axial electric field variations and enforced two-dimensionality. Cylinders of different diameters were placed both eccentrically and concentrically with the testbed axis to mimic different distributions of gas in a bubble column. For all cases, the conducting medium was deionized water with sodium chloride solution added to yield a conductivity of $\sigma = 420 \pm 5$ μS/cm. Data were acquired using both the PC software ('slow mode') and IC counters ('fast mode') to select electrode combinations.

Table 3
Effect of FEMEIT mesh refinement on reconstruction accuracy of a synthetic conductivity distribution[a]

Mesh	Computed σ	rms deviation in σ
A	0.679	0.170
B	0.676	0.027
C	0.669	0.007
D	0.666	0.003
E	0.666	0.003

[a] Analytical average of the synthetic distribution is $\sigma = 2/3$..

The following formula is used in the FEMEIT reconstructions for the spatial variation of conductivity $\sigma(x,y)$ in the case of a cylindrical insulator (Torczynski et al., 1996a):

$$\sigma = c_1\left\{1+\frac{p_1}{2}\left[\tanh\left(\frac{w-c_2}{p_2}\right)-\tanh\left(\frac{w+c_2}{p_2}\right)\right]\right\}, \tag{17}$$

where

$$w^2 = (x-c_3)^2+(y-c_4)^2. \tag{18}$$

This function represents a cylindrical region of radius c_2 centered at (c_3, c_4) with a boundary thickness proportional to $2p_2$. Well inside the region, the conductivity is approximately $c_1(1-p_1)$, and well outside, the conductivity is approximately c_1. When p_1 is slightly less than unity and p_2 is slightly less than the element size, this function represents an insulating cylinder of varying position and radius. Values of $p_1 = 0.99$ and $p_2 = 0.03$ were used here, and the resulting reconstructions were found to be insensitive to modest changes from these values.

Table 4 presents, for each test case, the actual diameter d of the test object and the offset distance z of the object center from the testbed central axis, both normalized by the domain radius R. The table also presents the normalized computed diameter $d/2R = c_2$ and offset distance $z/R = \sqrt{c_3^2 + c_4^2}$, determined from the EIT data. A domain-averaged volume fraction, $\bar{\varepsilon} = (d/2R)^2$, was also computed from the actual and reconstructed object dimensions. Fig. 8 shows the reconstructed conductivity distributions for two of the four test cases; the light areas indicate the object boundaries, numerical transition regions from high conductivity outside the object to zero conductivity within the object.

The reconstructions are in good agreement with actual conditions, reproducing the volume fraction to within 0.005 in $\bar{\varepsilon}$ and the distance of the inclusion from the central axis to within 3%. For the smaller inclusions the diameter of the object (and, hence, the average volume fraction) was always slightly overpredicted; in the case of the largest test object, the volume fraction was underpredicted. The source of the disagreement is believed to be differences between the measured and reconstructed voltages along the domain boundary. An example of these differences can be found by comparing the computed and experimental fundamental voltages in Table 1. While the computed voltages match the corrected experimental data to within 1% at each non-current-bearing electrode, changes in the sign and magnitude of the

Table 4
Comparison of actual and reconstructed geometries of insulating inclusions in two-dimensional validation tests

Actual conditions			PC electrode selection (slow mode)			IC electrode selection (fast mode)		
$d/2R$	z/R	$\bar{\varepsilon}$	$d/2R$	z/R	$\bar{\varepsilon}$	$d/2R$	z/R	$\bar{\varepsilon}$
0	–	0	0.062	0.000	0.004	0.059	0.000	0.004
0.266	0.596	0.071	0.271	0.597	0.074	0.271	0.597	0.074
0.300	0.000	0.090	0.309	0.020	0.095	0.308	0.020	0.095
0.534	0.189	0.285	0.530	0.184	0.281	0.530	0.184	0.280

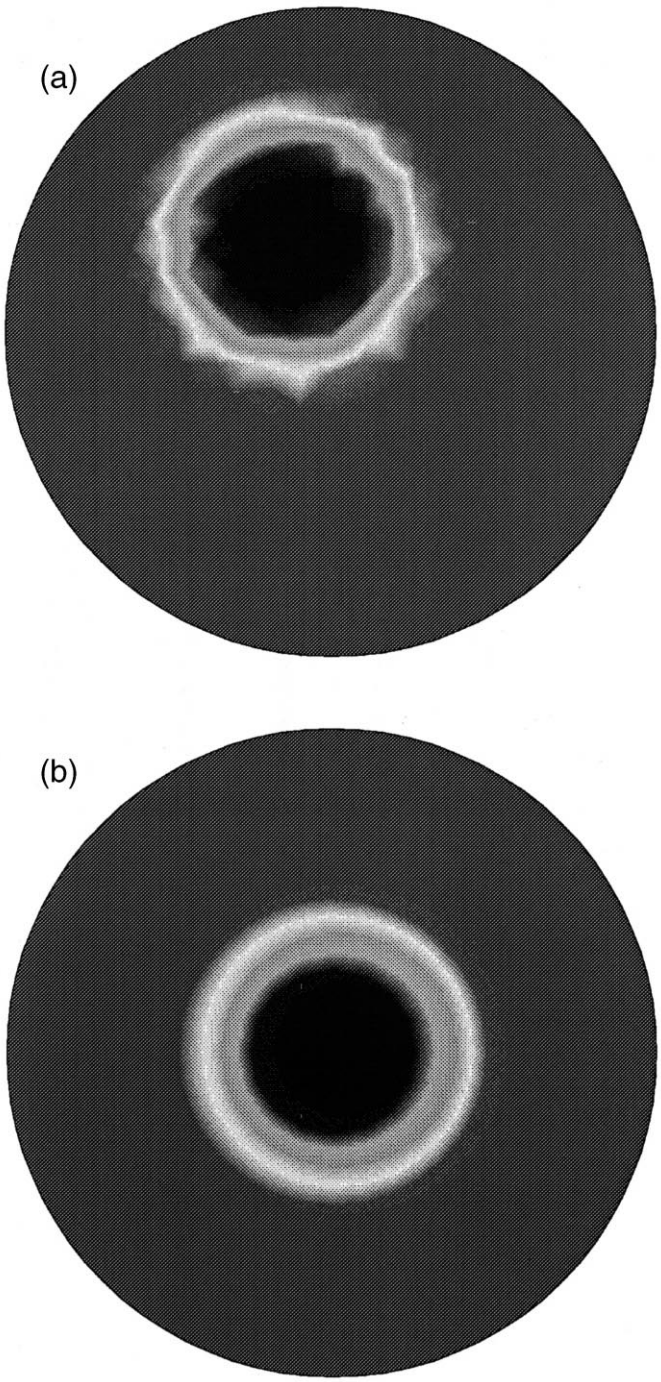

Fig. 8. Conductivity reconstructions for two-dimensional validation tests with inclusions: (a) $d = 5.07$ cm, $z = 5.68$ cm; (b) $d = 5.72$ cm, $z = 0.00$ cm.

difference indicate slightly different 'shapes' of the computed and experimental voltage profiles along the boundary. This would produce slight differences between the actual and reconstructed conductivity profiles.

Notably, the reconstruction algorithm produced a small object when none was present. This indicates that objects of diameters $d/2R \leq 0.06$ cannot be reconstructed, and that the uncertainty in $\bar{\varepsilon}$ is of the order of 0.004. This uncertainty is also attributed to slight differences between the computational and experimental boundary voltages for a uniform conductivity field, in the manner discussed above.

4. Experimental measurements of two-phase flows

The EIT system was applied to in situ measurement of dispersed two-phase flows. Both solid–liquid and gas–liquid flows were studied to determine the ability of EIT to measure volume-averaged phase fractions. In the solid–liquid tests, the size of the dispersed solid phase was much smaller than the size of the test vessel. In the gas–liquid bubbly flows, the size of the dispersed phase (air bubbles) was larger than in the solid–liquid mixture but still small compared to the scale of the apparatus.

The governing equation for the computational domain, Eq. (1), assumes no charge sources or sinks are present in the domain. For multiphase experiments, this assumption requires that no grounded conductors (except for the electrodes) may be in contact with the conducting medium anywhere within 10 column diameters of the electrode ring. To enforce this requirement, only electrically isolated instruments (cartridge heaters and thermocouples) were allowed at the flow boundaries, and mechanical devices within the flows were electrically isolated or given non-conducting coatings. The equation used to convert conductivity to liquid volume fraction, Eq. (7), requires an initial measurement of the liquid conductivity σ_L. The values of σ_L were determined in all experiments with the EIT system itself from measurements of the domain with only liquid present. A good measurement of liquid conductivity is crucial for obtaining quantitative data and requires careful control of test conditions, since conductivity can vary significantly with temperature and the presence of contaminants in the liquid.

4.1. Sandia GDT system

For validation of the EIT system in situ, phase distribution measurements were also made with a gamma-densitometry tomography (GDT) system developed at Sandia for studies of industrial-scale multiphase flows (Torczynski et al., 1996b; Shollenberger et al., 1997a). The GDT system employs a 5-curie ^{137}Cs gamma source, a sodium-iodide scintillation detector system, a computer-controlled traverse to position the source and detector, and data acquisition hardware and software. Measurements of gamma-ray attenuation are taken along many parallel beam paths and translated into a gamma attenuation coefficient, μ, averaged along each path. Attenuation by the testbed walls is subtracted from the raw data; then a time-averaged, normalized radial attenuation distribution is reconstructed using the Abel transform (Vest, 1985) and the assumption of an axisymmetric phase distribution. The axisymmetric

assumption is valid over the long acquisition time scales of GDT, which range from 15 to 30 min for gas–liquid flows. Attenuation profiles from the GDT system are routinely checked to verify that the axisymmetry assumption is valid.

For gas–liquid flows, the attenuation information may be converted to a gas volume fraction profile, ε_G, through the formula

$$\varepsilon_G^{GDT}(r,R) = \frac{\mu_L - \mu(r,R)}{\mu_L - \mu_G}, \tag{19}$$

where r is the radial coordinate, R is the radius of the circular domain, and the attenuation coefficients of the liquid and gas (μ_L and μ_G, respectively) have been previously measured or are known a priori. Since the attenuation distribution is axisymmetric, both the attenuation and phase distributions are modeled as polynomials with only even powers of r. By substituting an analytically averaged gamma attenuation coefficient, $\bar{\mu}$, for $\mu(r,R)$ in the equation, a domain-averaged phase volume fraction may also be obtained. In addition, the GDT system may be used for measurements of solid–liquid flows if the attenuation coefficients of the solid and liquid are significantly different.

4.2. Solid–liquid experiments

The first EIT validation experiment involved a closed container of conducting liquid with a flow of insulating solid particles. This solid–liquid flow was chosen for two reasons. First, the amount of solid introduced into the container can be carefully controlled, providing a good check of the tomography results. Second, unlike gas bubbles, solid particles can be small, uniform spheres that do not change shape during the experiment, so long as conditions are not harsh enough to fracture the particles.

Schematic diagrams of the experimental setup are shown in Fig. 9. The testbed consisted of the strip-electrode cylinder stacked between two Lexan cylinders of the same inner diameter and wall thickness. This testbed, 81.3 cm in height, was capped at the bottom and the top, and a 1.5-W Sargent–Welch mixer was inserted into the cylinder through a small hole in the center of the top cap. The mixer was used to generate a relatively uniform solids distribution inside the cylinder; to prevent settling of the solids, the mixer impeller was positioned 1.27 cm above the lower cap. Since the mixer's shaft was not long enough to reach out of the cylinder, an insulating Lexan extender joined the end of the shaft to a second shaft connected to the Sargent–Welch mixer motor mounted above the testbed. An 'overflow' volume was placed above the top cap to eliminate free-surface effects — e.g., a vortical 'funnel' — in the cylinder interior during mixing.

Although the mixer shaft was small compared to the test cylinder (the ratio of their diameters was 0.042), the presence of the shaft posed problems for EIT. Placing an electrical conductor in the center of the testbed had the potential to significantly distort the electric field lines, so the steel shaft and impeller were coated with a layer of insulating paint to mitigate this effect. Earlier EIT measurements with and without the mixer shaft in place, with no particles present, verified that the insulated shaft had only a small effect on EIT behavior (Shollenberger et al., 1997b).

As discussed above, the liquid phase was deionized water with a small amount of saturated sodium nitrate solution added for conductivity control. For the solid phase, polystyrene spheres with a density of 1.04 g/cm^3 and a range of diameters from 200 to 700 μm were used. Polystyrene is an insulator with respect to water, so EIT is able to discriminate between the solid and liquid phases. EIT measurements were compared to the nominal cylinder-averaged solid volume fraction $\bar{\varepsilon}_S^{NOM}$, computed from the density and total mass of polystyrene added to the testbed. GDT is not useful in this case because the attenuation coefficients of polystyrene and water are too similar for the phases to be distinguished: $\mu_L = 0.0856$ cm^{-1}, $\mu_S = 0.0866$ cm^{-1} (Thoraeus, 1965). Insulating solids that have attenuation coefficients significantly different

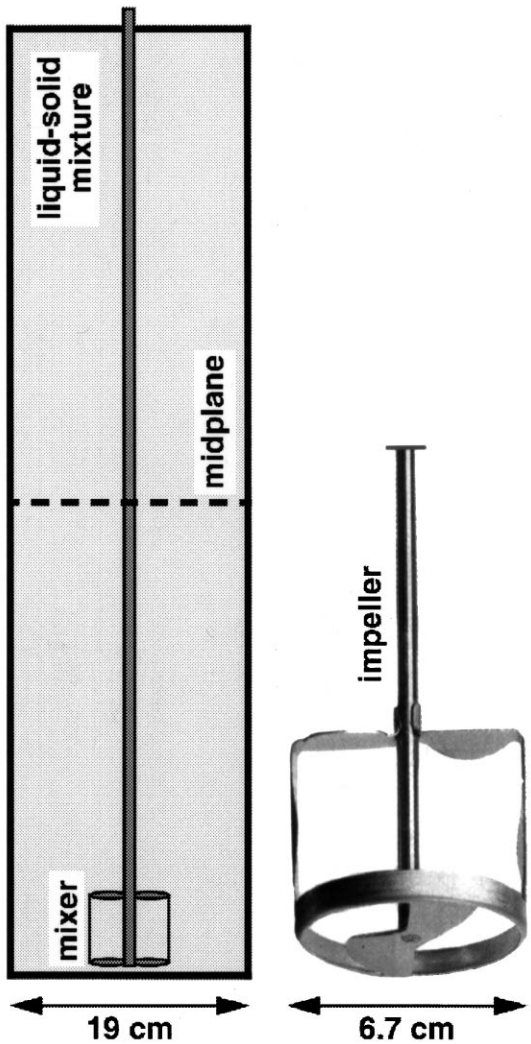

Fig. 9. Schematic diagram of test geometry for the solid–liquid experiments, showing the impeller geometry and location within the testbed.

from water typically have a much higher specific gravity and are difficult to loft uniformly (Shollenberger et al., 1997b).

For each value of $\bar{\varepsilon}_S^{NOM}$, the required mass of spheres was introduced into the testbed, and liquid was added to occupy the remaining volume. A mixer speed of 420 rpm was applied for 30 min to all solid loadings, with the result that a roughly uniform distribution of particles was observed visually within the liquid during measurements. EIT voltage measurements were repeated over the 30-min stirring period to verify that a steady-state distribution had been attained. Mixing was then terminated, and the spheres were allowed to settle to the bottom of the cylinder. Following this settling period, EIT was applied again. The second EIT measurement was necessary to determine a baseline liquid conductivity; despite attempts to wash and rinse the polystyrene particles before the experiments, soluble contaminants were introduced with the particles that altered the conductivity of the water. The magnitude of this effect on the water conductivity was comparable to that of the suspended solid particles during mixing. Changes in water temperature and associated changes in conductivity were negligible during mixing.

Analysis of the data with EITAXI demonstrated that radial variations in the local solids density ε_S were less than 0.01 across the domain, and thus the radial solids profiles were uniform to within experimental uncertainty. The radial data were analytically integrated to obtain cross-sectionally-averaged solid volume fractions $\bar{\varepsilon}_S^{EIT}$, which are plotted in Fig. 10. The solid volume fractions determined by EIT are seen to be in close agreement in all cases with the nominal values computed from the mass of added particles, validating the method for solid–liquid measurements. The difference between measured and nominal values becomes more negative with increasing solid volume fraction, approaching $\bar{\varepsilon}_S^{EIT} - \bar{\varepsilon}_S^{NOM} = -0.003$ when $\bar{\varepsilon}_S^{NOM} = 0.050$. It is possible that the ability of the mixer to produce a uniform axial distribution

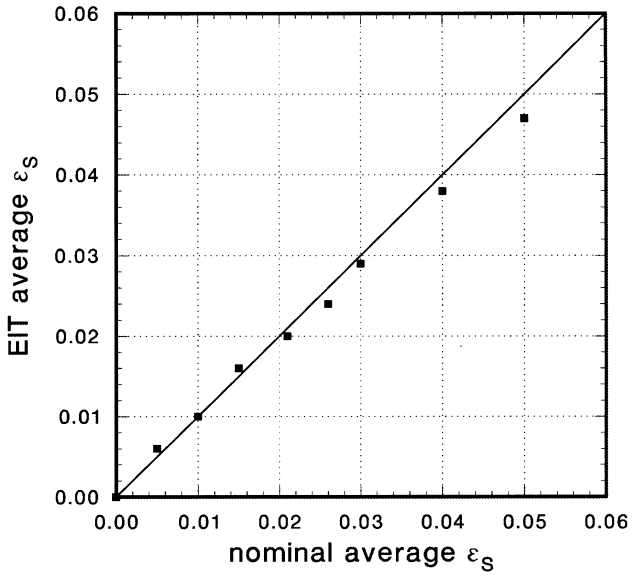

Fig. 10. Solid volume fractions measured by EIT in solid–liquid mixtures.

dropped with increased solid loadings, so that the solid volume fraction was slightly less than the nominal value near the top of the cylinder and slightly larger at the bottom. Another explanation for this trend is that a small amount of solids was observed escaping through the hole in the top cap during stirring. These solids passed into the overflow volume, reducing the actual amount of solids in the measurement volume. The fraction of total solids lost to the overflow volume was observed to increase with nominal loading, possibly causing the observed trend.

4.3. Gas–liquid experiments

Gas–liquid tests of the EIT system were conducted in a transparent bubble column assembled at Sandia as a testbed for optical, electrical, and radiation-based multiphase flow diagnostics (Torczynski et al., 1997). The Lexan column, shown in Fig. 11 with the GDT system in place, has an inner diameter D of 19.05 cm, a wall thickness of 0.64 cm, and is built from interchangeable sections so that different diagnostic tools can be placed in the column. In this study, the EIT electrode section was placed near the center of the column. The 16 strip electrodes were centered on a plane $L = 97.16$ cm above the base, at a height-to-diameter ratio of $L/D = 5.1$. The column was filled with water to a depth H_0 of 1.45 m, for a height-to-diameter ratio of 7.6; this depth placed the region of EIT sensitivity completely under water. Air can be introduced at volumetric flow rates up to 10,000 cm^3/s through one of several interchangeable spargers at the base of the column. The spargers are electrically isolated to prevent interference with the EIT system. The column operates at ambient conditions, but the water is subject to evaporative cooling as air is bubbled through; the liquid temperature was held constant by active heating to within $\pm 0.2^{\circ}C$ during experiments, which limited variations in conductivity with temperature to $\pm 0.3\%$.

The goal for the gas–liquid tests was to validate EIT against GDT in a flow with variations on a larger scale than the solid–liquid flows. A comparison of the two methods was made in churn-turbulent flows in a vertical column; such flows normally have time-averaged volume fraction profiles that are approximately parabolic and can, therefore, be reconstructed by both the GDT and EIT algorithms. A discussion of the influences of temporal flow variations on GDT and EIT reconstruction uncertainties is deferred to the end of this section.

The sparger used to produce churn-turbulent flows is shown in Fig. 12. This sparger is a hollow stainless steel toroid with a 10.16-cm centerline diameter, an inner tube diameter of 0.95 cm, and 10 holes of diameter 0.16 cm facing downward. Churn-turbulent experiments were performed using five flow rates: 420, 830, 1250, 1670 and 2500 cm^3/s. The corresponding superficial gas velocities range from 1.5 to 8.8 cm/s. Fig. 13 shows the flow conditions in the column for the minimum and maximum flow rates. At the lowest flow condition, a range of bubble sizes was evident, as was a central helical bubble stream. At rates of 1250 cm^3/s and above, the flow was completely opaque and turbulent to the naked eye. For each flow condition, 25 full EIT projection sets taken over a period of less than 20 s were averaged to obtain the voltage data for reconstructions. Multiple data sets were averaged to enable direct comparison with GDT results, which are inherently time-averaged, and to allow use of axisymmetric reconstruction algorithms. The conductivity of the water used in the gas–liquid

experiments was 285 ± 5 μS/cm. GDT measurements were taken in a plane 81.0 cm above the column floor ($L/D = 4.25$), a location chosen to avoid obstruction by the electrodes.

In the EIT reconstructions, the three-dimensional algorithm was used with the assumption of the parabolic profile given by Eq. (6). Similarly, chord-averaged attenuation coefficients computed from GDT data were fit to a second- or fourth-order polynomial before the Abel transform was taken. The choice of polynomial for each fit was made based upon the least-

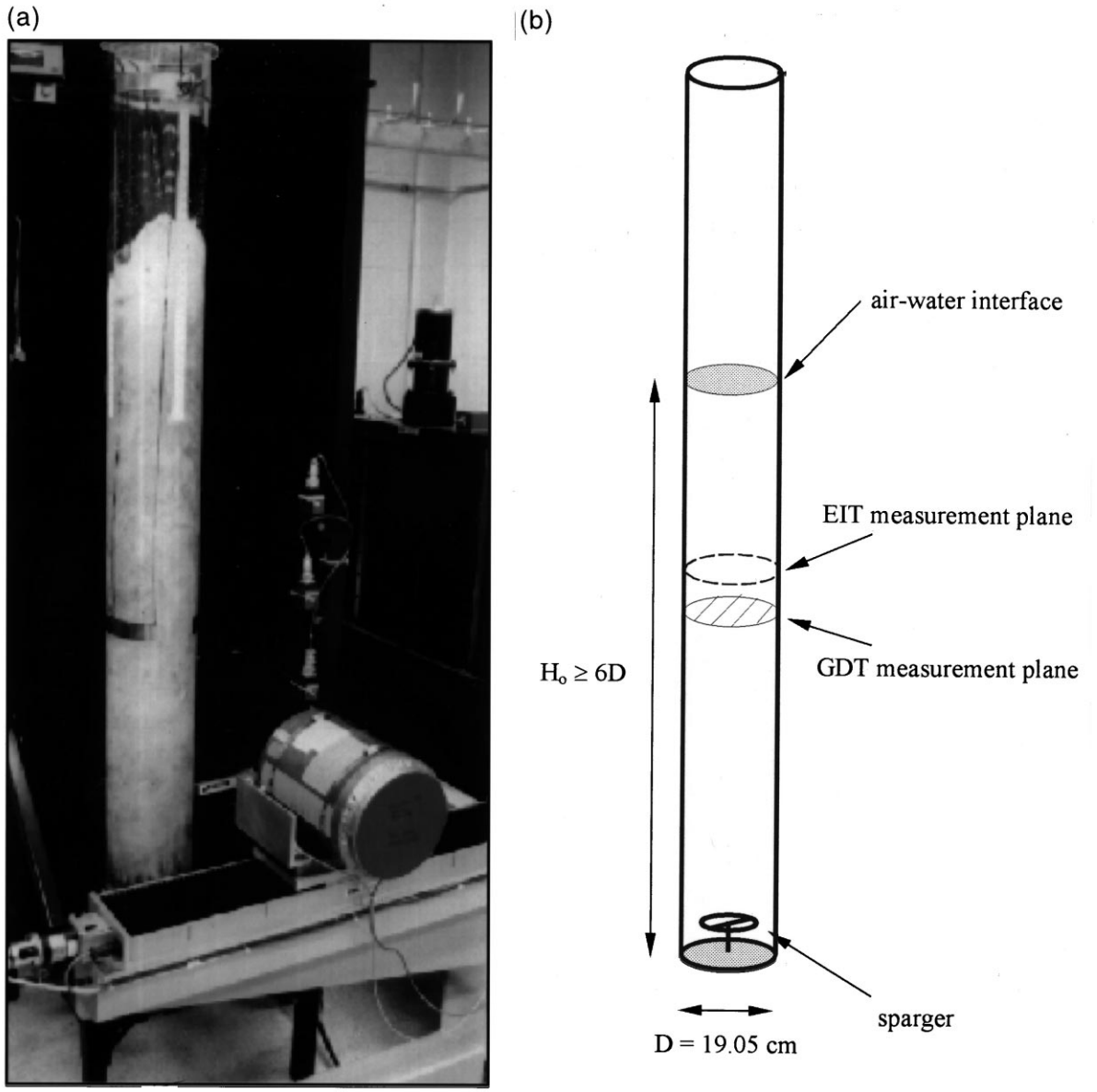

Fig. 11. Lexan bubble column (19 cm I.D.) used in churn-turbulent flow experiments: (a) photograph of column with Sandia GDT system in place; (b) schematic diagram of column indicating measurement locations.

squares error between the fit and the attenuation data. Fig. 14 shows the gas volume profiles measured by both methods for all volumetric flow rates. The EIT profile tends to lie slightly above the GDT profile at each flow rate; however, the GDT and EIT gas volume fractions are in excellent agreement, falling within 0.01 of each other at all radial positions. Since the change in the local volume fraction across the column is as large as 0.20, this level of agreement strongly validates the EIT method. Values of $\bar{\varepsilon}_G$ were also determined from EIT and GDT by analytically averaging the profiles of Fig. 14 over the column area. Fig. 15 shows these cross-sectionally-averaged gas volume fractions as a function of superficial gas velocity U_G. Again, the GDT and EIT values are in very good agreement, differing by no more than 0.01 in $\bar{\varepsilon}_G$. This degree of consistency between GDT and EIT suggests that both methods are accurate for measuring axisymmetric profiles so long as temporal-averaging effects are benign.

To assess the effect of temporal averaging on the EIT and GDT reconstructions, separate flow measurements were taken under the same churn-turbulent flow conditions with an impedance-based bulk void fraction meter described in detail by Torczynski et al. (1997). This instrument has two rectangular electrodes 3.8 cm high, which subtend 120° each on opposite sides of the column (see Fig. 16). An impedance phase meter circuit operating at 50 kHz is used to excite the bulk void fraction meter, and the voltage across the electrodes is recorded with a digitizing oscilloscope for analysis of fluctuations in gas volume fraction. The meter is capable of detecting fluctuations with time scales on the

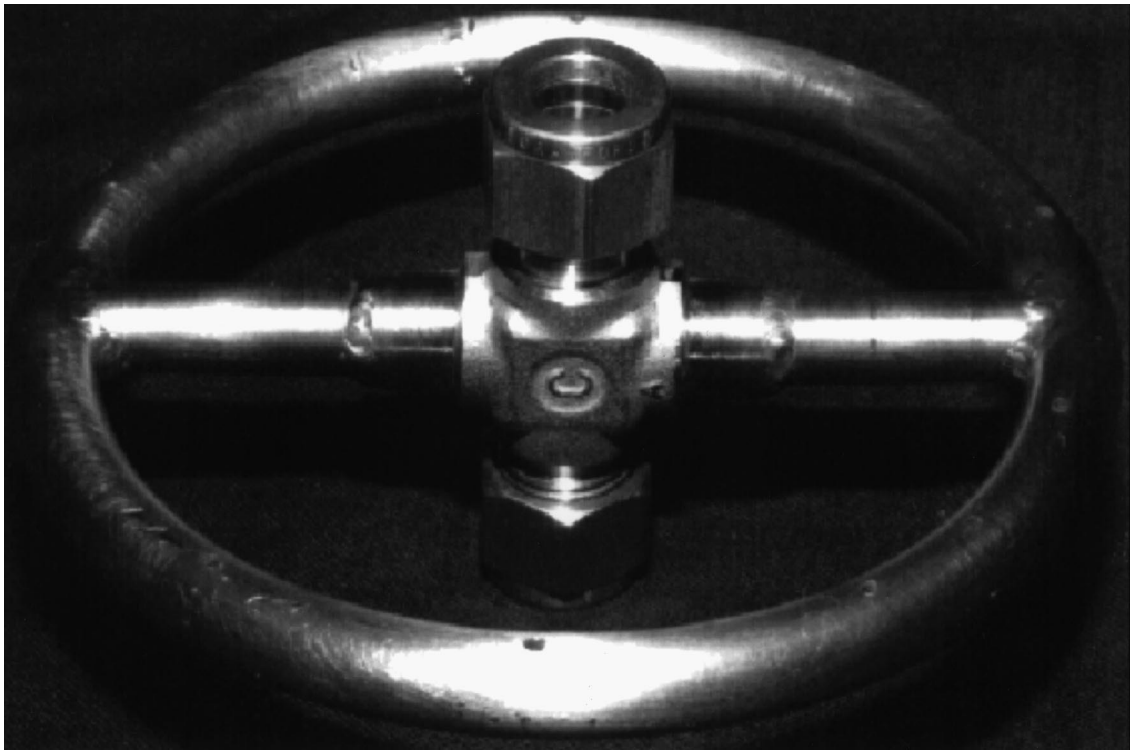

Fig. 12. Ring sparger used in churn-turbulent flow experiments.

Fig. 13. Churn-turbulent flow conditions in the transparent bubble column at minimum and maximum volumetric flow rates: (a) $Q = 420$ cm^3/s, (b) 2500 cm^3/s. The vertical scale is in centimeters.

Fig. 13 (*continued*)

order of 40 μs. Since the time scales for churn-turbulent flows in the bubble column are expected to be much larger than this value, the meter can resolve temporal variations in the flow.

Because of the difference in collection times for the two methods (about 23 min for GDT

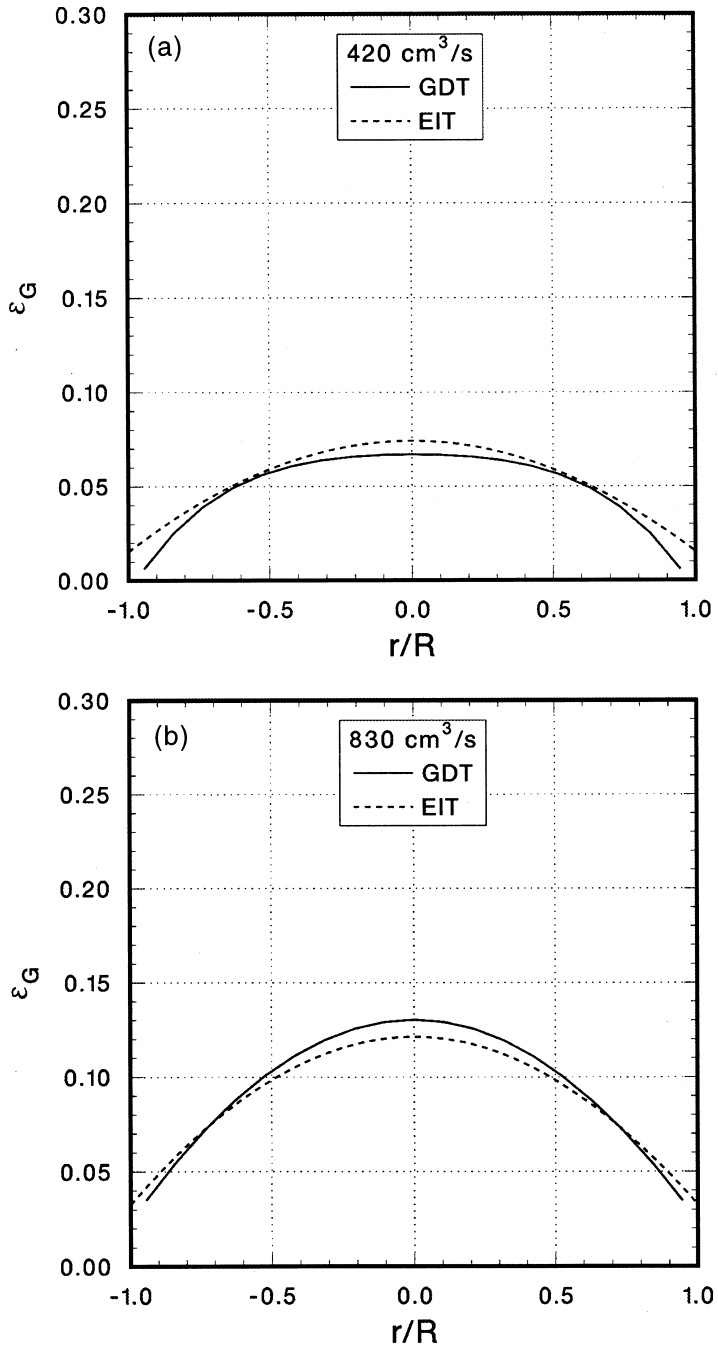

Fig. 14. Comparisons of symmetric radial gas volume fraction profiles from GDT and EIT.

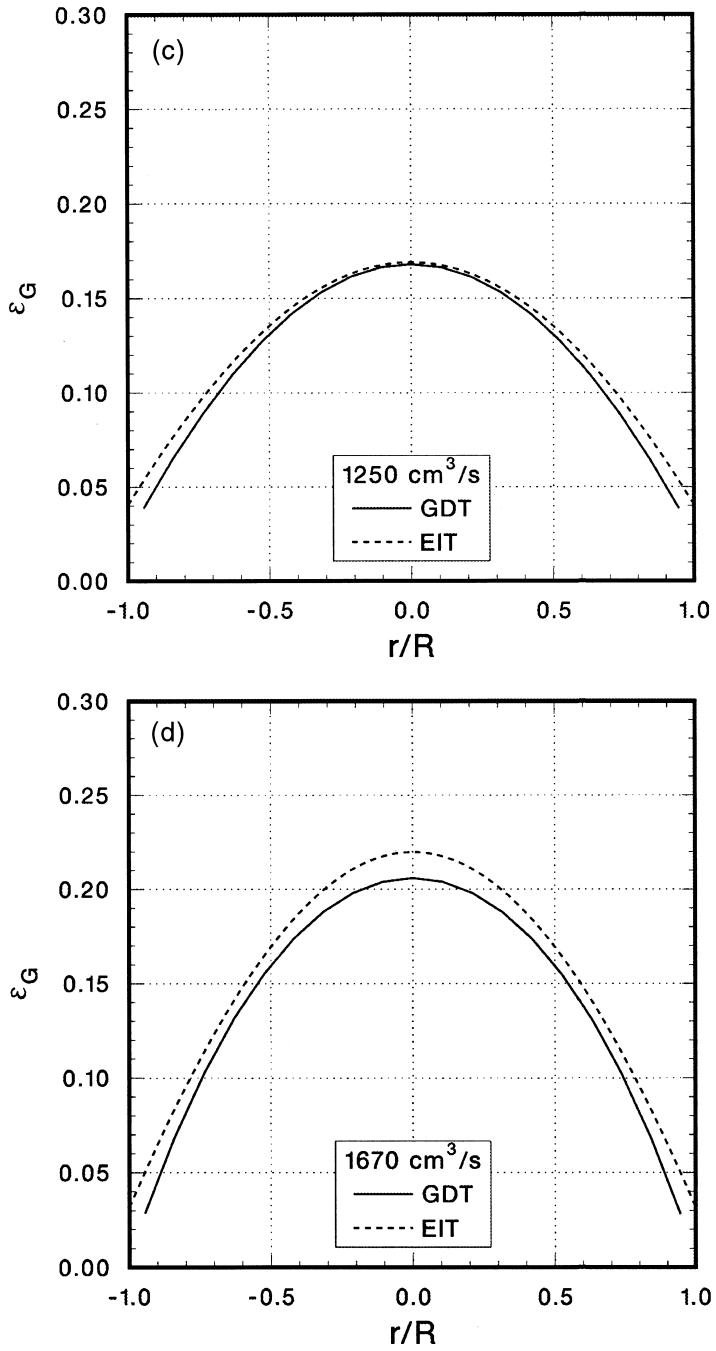

Fig. 14 (*continued*)

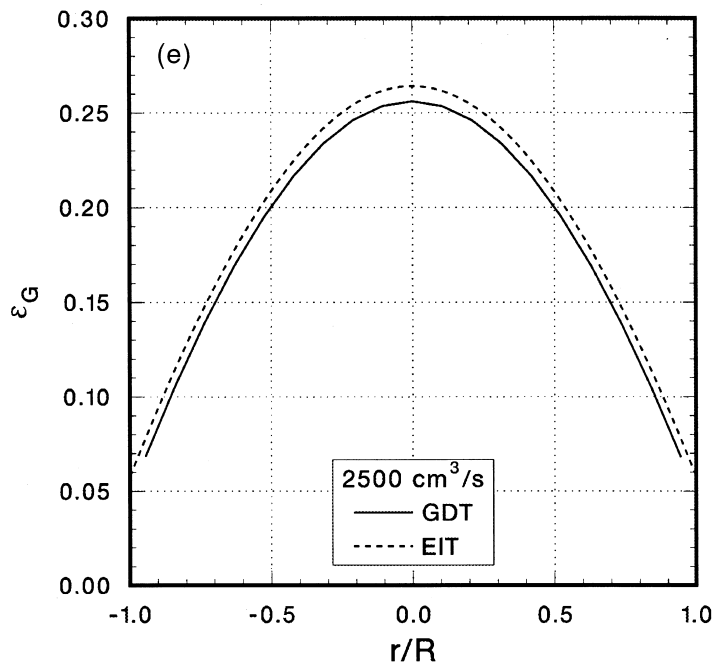

Fig. 14 (*continued*)

but less than 20 s for EIT), it was decided to look for slow oscillations in the flows with the bulk void fraction meter which might be averaged out by GDT but not by EIT. The voltage across the bulk meter electrodes was recorded over a period of 10 min with a digitizing oscilloscope, and Fourier spectra were computed from the data to determine the frequencies of gas volume fraction fluctuations. Signal spectra revealed no coherent periodic flow behavior over the range of zero to 12.5 Hz; this alleviated the concern that EIT measurements were capturing data over only a portion of slow flow cycles. This conclusion has also been substantiated using differential-pressure measurements to estimate gas volume fraction in the fully developed flow region.

The bulk meter voltage signals were further analyzed to estimate variations in gas volume fraction for all flow conditions. Using a sum-of-squares method, the rms voltage variation measured without gas flow was subtracted from the rms variation at each flow condition to estimate variations in the signals solely due to variations in gas volume fraction. Average voltages $\bar{V}$ were correlated with cross-sectionally-averaged gas volume fractions $\bar{\varepsilon}_G$ determined from concurrent GDT scans, and temporal variations in $\bar{\varepsilon}_G$ at each flow condition were estimated from the voltage variations and the correlation of $\bar{\varepsilon}_G$ vs. $\bar{V}$. Table 5 compares $\Delta\bar{\varepsilon}_G^{Bulk}$, the estimate of these temporal variations, with $\bar{\varepsilon}_G^{EIT} - \bar{\varepsilon}_G^{GDT}$, the difference between the average values measured by EIT and GDT. Since $\Delta\bar{\varepsilon}_G^{Bulk}$ and $\bar{\varepsilon}_G^{EIT} - \bar{\varepsilon}_G^{GDT}$ are comparable, the different methods of temporal averaging by EIT and GDT may account for some of the difference between the two measured average values. However, since the differences $\bar{\varepsilon}_G^{EIT} - \bar{\varepsilon}_G^{GDT}$ and $\Delta\bar{\varepsilon}_G^{Bulk}$ are small compared to both $\bar{\varepsilon}_G^{EIT}$ and $\bar{\varepsilon}_G^{GDT}$, both methods

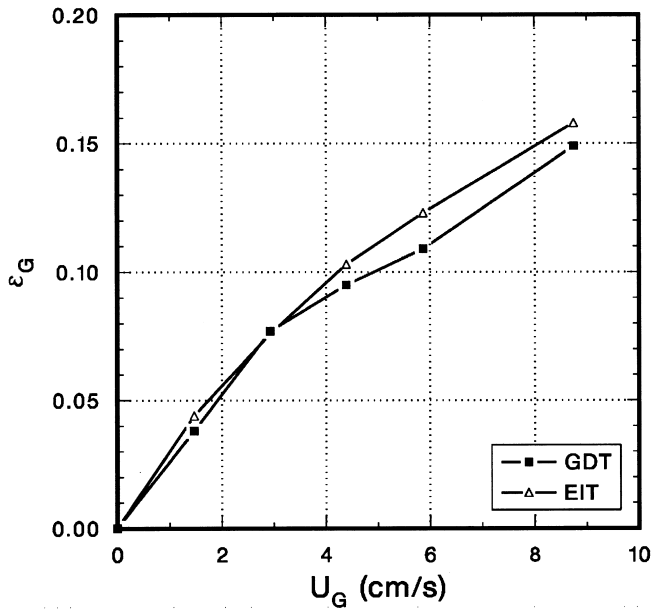

Fig. 15. Comparison of cross-sectionally-averaged gas volume fractions measured by GDT and EIT.

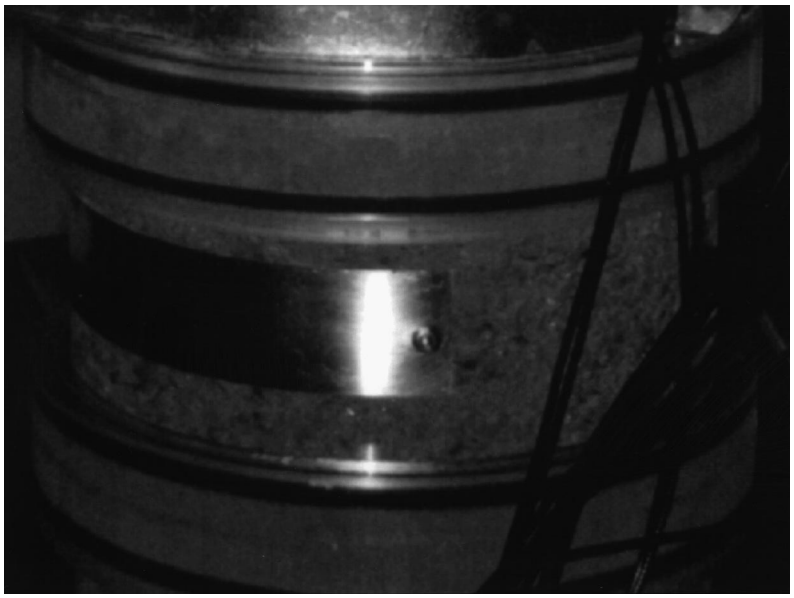

Fig. 16. Impedance-based bulk void fraction meter used to investigate fluctuations in gas volume fraction.

Table 5
Comparison of differences between EIT and GDT with temporal fluctuations in gas volume fraction measured by the bulk void fraction meter

U_G (cm/s)	$\bar{\varepsilon}_G^{EIT}$	$\bar{\varepsilon}_G^{GDT}$	$\bar{\varepsilon}_G^{EIT} - \bar{\varepsilon}_G^{GDT}$	$\Delta\bar{\varepsilon}_G^{Bulk}$
1.5	0.044	0.038	0.006	0.015
2.9	0.076	0.077	−0.001	0.016
4.4	0.103	0.095	0.008	0.018
5.9	0.123	0.109	0.014	0.020
8.8	0.158	0.149	0.009	0.023

of temporal averaging appear to be benign. Future investigations will examine the effects of temporal averaging by EIT and GDT more closely.

5. Conclusions

The Sandia Michigan EIT system has been validated for the measurement of solid volume fractions in solid–liquid flows, and gas volume fractions and radial profiles in gas–liquid flows. EIT was used to measure solid volume fractions of up to 0.05, with excellent agreement between EIT results and the nominal values determined from the mass of solids in each flow. Gas–liquid bubble-column flows were measured with EIT and GDT; for cross-sectionally-averaged gas volume fractions up to 0.15, the average values and radial profiles from EIT and GDT agreed to within 0.01, despite large radial variations across the column. The Maxwell–Hewitt relations used to convert conductivity information to conducting phase distributions were found to be accurate for cases where the assumptions inherent in their derivation were valid.

Future work will extend the use of EIT and GDT to three-phase flows in a slurry bubble column, so that the effect of the solid phase on hydrodynamic behavior may be examined. The study will employ a solid phase with conductive properties similar to air and a density similar to water, so that EIT will detect both the solid and gas phases but GDT will detect only the gas phase. The difference in the radial profiles from the two reconstruction methods will yield a radial solids distribution in the three-phase flow. This will represent another step toward the application of EIT to industrial multiphase flows.

Acknowledgements

This work was performed at Sandia National Laboratories. Sandia is a multiprogram laboratory operated by Sandia Corporation, a Lockheed Martin Company, for the United States Department of Energy under Contract DE-AC04-94AL85000. A portion of this work was funded by the Federal Energy Technology Center under Field Work Proposal FEW 8616. The authors are grateful for technical interactions with B.A. Toseland of Air Products and Chemicals. The authors would also like to thank C.B. Lafferty and W.C. Ginn for their skilled

technical assistance, D.R. Adkins for his early work with the GDT system, and A.T. Leger for her early work with the EIT system. The reviewers of this article are also gratefully acknowledged for their helpful comments.

References

Adkins, D.R., Shollenberger, K.A., O'Hern, T.J., Torczynski, J.R., 1996. Pressure effects on bubble column flow characteristics. In: ANS Proceedings of the 1996 National Heat Transfer Conference, THD-Vol. 9, 318–325.

Ceccio, S.L., George, D.L., 1996. A review of electrical impedance techniques for the measurement of multiphase flows. J. Fluids Eng. 118, 391–399.

Dickin, F.J., Williams, R.A., Beck, M.S., 1993. Determination of composition and motion of multicomponent mixtures in process vessels using electrical impedance tomography. Part I: principles and process engineering applications. Chem. Eng. Sci. 48, 1883–1897.

Duraiswami, R., Chahine, G.L., Sarkar, K., 1997. Boundary element techniques for efficient 2-D and 3-D electrical impedance tomography. Chem. Eng. Sci. 52, 2185–2196.

Fluid Dynamics International, 1995. FIDAP Users Manual. Fluid Dynamics International, Evanston, IL.

George, D.L., Ceccio, S.L., Shollenberger, K.A., Torczynski, J.R., O'Hern, T.J., 1998. Comparison of electrical-impedance tomography and gamma-densitometry tomography for the measurement of gas volume fraction profiles in a bubble column. In: Proceedings of the 1998 ASME Fluids Engineering Division Summer Meeting, FED-Vol. 245, No. 98–5081.

Hewitt, G.F., 1978. Measurement of Two-Phase Flow Parameters. Academic Press, London.

Huang, S.M., Plaskowski, A.B., Xie, C.G., Beck, M.S., 1989. Tomographic imaging of two-component flow using capacitance sensors. J. Phys. E: Sci. Instr. 22, 173–177.

Jackson, N.B., Torczynski, J.R., Shollenberger, K.A., O'Hern, T.J., Adkins, D.R., 1996. Hydrodynamic characterization of slurry bubble-column reactors for Fischer–Tropsch synthesis. In: Proceedings of the Thirteenth Annual International Pittsburgh Coal Conference, Vol. 2: Coal-Energy and the Environment, 1226–1231.

Jones, O.C., Lin, J.-T., Ovacik, L., 1992. Investigation of electrical impedance imaging relative to two-phase, gas–liquid flows. Chem. Eng. Comm. 118, 299–325.

Jones, O.C., Lin, J.-T., Ovacik, L., Shu, H., 1993. Impedance imaging relative to gas–liquid systems. Nucl. Eng. Design 141, 159–176.

Jones, O.C., Lin, J.-T., Shu, H., Ovacik, L., He, Y., 1994. Impedance imaging relative to binary mixtures. In: Fifth International Symposium on Liquid–Solid Flows. American Society of Mechanical Engineers, New York.

Maxwell, J.C., 1881. A Treatise on Electricity and Magnetism. Clarendon Press, Oxford, England.

O'Hern, T.J., Torczynski, J.R., Ceccio, S.L., Tassin, A.L., Chahine, G.L., Duraiswami, R., Sarkar, K., 1995. Development of an electrical-impedance tomography system for an air–water vertical bubble column. In: ASME Forum on Measurement Techniques in Multiphase Flows, FED-Vol. 233, 531–537.

Plaskowski, A., Beck, M.S., Thorn, R., Dyakowski, T., 1995. Imaging Industrial Flows: Applications of Electrical Process Tomography. Institute of Physics Publishing, Bristol, England.

Reinecke, N., Mewes, D., 1997. Multielectrode capacitance sensors for the visualization of transient two-phase flows. Exp. Thermal Fluid Sci. 15, 253–266.

Shollenberger, K.A., Torczynski, J.R., Adkins, D.R., O'Hern, T.J., Jackson, N.B., 1997a. Gamma-densitometry tomography of gas holdup spatial distribution in industrial-scale bubble columns. Chem. Eng. Sci. 52, 2037–2048.

Shollenberger, K.A., Torczynski, J.R., O'Hern, T.J., Adkins, D.R., Ceccio, S.L., George, D.L., 1997b. Comparison of gamma-densitometry tomography and electrical-impedance tomography for determining material distribution in liquid-solid flows. In: Proceedings of the 1997 ASME Fluids Engineering Division Summer Meeting, Vol. FEDSM '97, No. 97-3690.

Somersalo, E., Cheney, M., Isaacson, D., 1992. Existence and uniqueness for electrode models for electric current computed tomography. SIAM J. Appl. Math. 52, 1023–1040.

Thoraeus, R., 1965. Attenuation of gamma radiation from ^{60}Co, ^{137}Cs, ^{192}Ir, and ^{226}Ra in various materials used in radiology. Acta Radiologica 3, 81–86.

Torczynski, J.R., O'Hern, T.J., Shollenberger, K.A., Ceccio, S.L., Tassin, A.L., 1996a. Finite element method electrical-impedance tomography for phase distribution determination in multiphase flows: validation calculations and experiments. In: ASME Cavitation and Multiphase Flow Forum, FED-Vol. 236, 497–501.

Torczynski, J.R., Adkins, D.R., Shollenberger, K.A., O'Hern, T.J., 1996b. Application of gamma-densitometry tomography to determine phase spatial variation in two-phase and three-phase bubbly flows. In: ASME Cavitation and Multiphase Flow Forum, FED-Vol. 236, 503–508.

Torczynski, J.R., O'Hern, T.J., Adkins, D.R., Jackson, N.B., Shollenberger, K.A., 1997. Advanced tomographic flow diagnostics for opaque multiphase fluids. Report SAND97-1176, Sandia National Laboratories, Albuquerque, NM.

Vest, C.M., 1985. Tomography for properties of materials that bend rays: a tutorial. Appl. Opt. 24, 4089–4094.

Webster, J.G. (Ed.), 1990. Electrical Impedance Tomography. Adam Hilger, Bristol, England.

Yorkey, T.J., Webster, J.G., Tompkins, W.J., 1987. Comparing reconstruction methods for electrical impedance tomography. IEEE Trans. Biomedical Eng. 11, 843–852.